

Machine learning aided parameter analysis in Perovskite X-ray Detector

Bobo Zhang^{1†}, Endai Huang^{2,3†}, Xinyi Du^{4,5}, Xiaokang Ma⁶, Lu Zhang¹, Jiaxue You^{7*},
Alex K.Y. Jen^{7*} and Shengzhong (Frank) Liu^{1,8,9*}

¹Key Laboratory of Applied Surface and Colloid Chemistry, Ministry of Education; Shaanxi Key Laboratory for Advanced Energy Devices; Shaanxi Engineering Lab for Advanced Energy Technology; Institute for Advanced Energy Materials; School of Materials Science and Engineering, Shaanxi Normal University, Xi'an 710119, China.

²Research Institute of Medical and Biological Engineering, Ningbo University, Zhejiang 315211, China

³Department of Computer Science and Engineering, The Chinese University of Hong Kong, Hong Kong SAR 999077, China

⁴Department of Chemical and Biomolecular Engineering, National University of Singapore, Singapore, Singapore.

⁵Solar Energy Research Institute of Singapore (SERIS), National University of Singapore, Singapore, Singapore.

⁶State Key Laboratory of Solidification Processing, Northwestern Polytechnical University, Xi'an, Shaanxi 710072, PR China.

⁷Department of Materials Science and Engineering, Hong Kong Institute for Clean Energy City University of Hong Kong, Hong Kong SAR 999077, China

⁸Dalian National Laboratory for Clean Energy; iChEM, Dalian Institute of Chemical Physics, Chinese Academy of Sciences, Dalian 116023, China.

⁹University of the Chinese Academy of Sciences, Beijing 100039, China.

†: BZ and EH contributed equally.

Corresponding authors*: JY: jjaxuyou@cityu.edu.hk, AJ: alexjen@cityu.edu.hk, SL: szliu@dicp.ac.cn.

ABSTRACT: Many factors in perovskite X-ray detectors, such as crystal lattice and carrier dynamics, determine the final device performance (e.g., sensitivity and detection limit). However, the relationship between these factors remains unknown due to the complexity of the material. In this study, we employ machine learning to reveal the

relationship between 15 intrinsic properties of halide perovskite materials and their device performance. We construct a database of X-ray detectors for the training of machine learning. The results show that the band gap is mainly influenced by the atomic number of the B-site metal, and the lattice length parameter b has the greatest impact on the carrier mobility-lifetime product ($\mu\tau$). An X-ray detector $(\text{m-F-PEA})_2\text{PbI}_4$ were generated in the experiment and it further verified the accuracy of our ML models. We suggest further study on random forest regression for X-ray detector applications.

KEY WORDS:

X-ray detector, machine learning, lattice parameters, carrier dynamics, dark current.

1. Introduction

X-ray detectors play a vital role in various fields such as nuclear physics and technology, medical diagnostics, non-destructive testing, security inspections, astronomical observations, and high-energy physics research¹. Halide perovskites have emerged as a promising candidate for X-ray detection due to their exceptional photoelectric properties, including a large atomic number for high absorption coefficient, a large carrier mobility-lifetime product ($\mu\tau$) for efficient charge collection, and adjustable band gaps leading to low leakage currents^{2, 3}. The performance evaluation of X-ray detectors relies heavily on parameters such as sensitivity, detection limit, and dark current⁴. For applications like medical imaging, maintaining exceptional sensitivity and a low detection limit is crucial to minimize radiation exposure. Additionally, these detectors must exhibit dark current densities below 1 nA cm^{-2} to uphold high detection quantum efficiency and dynamic range.⁵ Researchers have concentrated on material design, particularly focusing on A-site cations⁶⁻¹³, B-site ions¹⁴⁻¹⁹, and X-site anions regulation^{20, 21}.

Utilizing three-dimensional (3D) perovskite materials has enabled X-ray detectors to achieve outstanding performance metrics²², although challenges with dark current density persist. Modifying the A-site cations and exploring lower-dimensional structures have shown promise in reducing dark currents²³. While low-dimensional perovskites exhibit high resistivity and lower dark currents, they may face limitations in carrier transport that impact X-ray responsiveness compared to 3D detectors²⁴.

Researchers have been striving to enhance the performance and stability of perovskite detectors through various methods, including material synthesis, crystal optimization, and novel fabrication techniques. Despite efforts to improve sensitivity and reduce dark current density, achieving high sensitivity, low detection limits, and minimal dark currents below 1 nA cm^{-2} remains a significant engineering hurdle due to the inherent properties of perovskite materials and technological complexities. In addition, the key parameter affecting dark current remains unknown, due to the complexity of parameter analysis. There are many parameters involved, such as atomic number, lattice constant, trap density (Trap), bandgap (E_g), time-resolved photoluminescence (TRPL), resistivity (RT), and carrier mobility-lifetime product ($\mu\tau$) etc.

Machine learning (ML) technology has recently shown promising advancements in the realm of new energy materials design and analysis, particularly in optimizing solar cells, predicting band gaps, designing compositions, and screening lead-free alternatives²⁵⁻²⁸. ML's ability to extract information from complex datasets autonomously can aid in identifying patterns and optimizing key parameters for improved detector performance by linking material properties to detector characteristics affected by multiple factors. Integrating ML methodologies could offer a novel approach to addressing these complex systems and predicting X-ray detector performance.

To this end, this study integrates ML into predicting X-ray detector performance. The workflow is as follows. Initially, feature parameters (Z_A , Z_B , Z_X , Z_{total} , a, b, c, α , β , γ , E_g , $\mu\tau$, TRPL, Trap, RT, detection limit, and sensitivity) are derived from existing literature. During this process, missing values are estimated using comparable values from other literature sources. Subsequently, the suggested characteristic parameters are normalized to ensure scale uniformity and enhance convergence speed. Furthermore, five ML algorithms, namely multivariable linear regression (MLR), random forest regression (RFR), eXtreme Gradient Boosting (XGBoost), support vector regression (SVR), and symbolic regression based on genetic programming (GPSR) are then employed to determine the weights of the characteristic parameters that influence E_g , $\mu\tau$, sensitivity, and detection limit. Ultimately, a novel X-ray detector device is

fabricated to validate the model's accuracy in real-world applications.

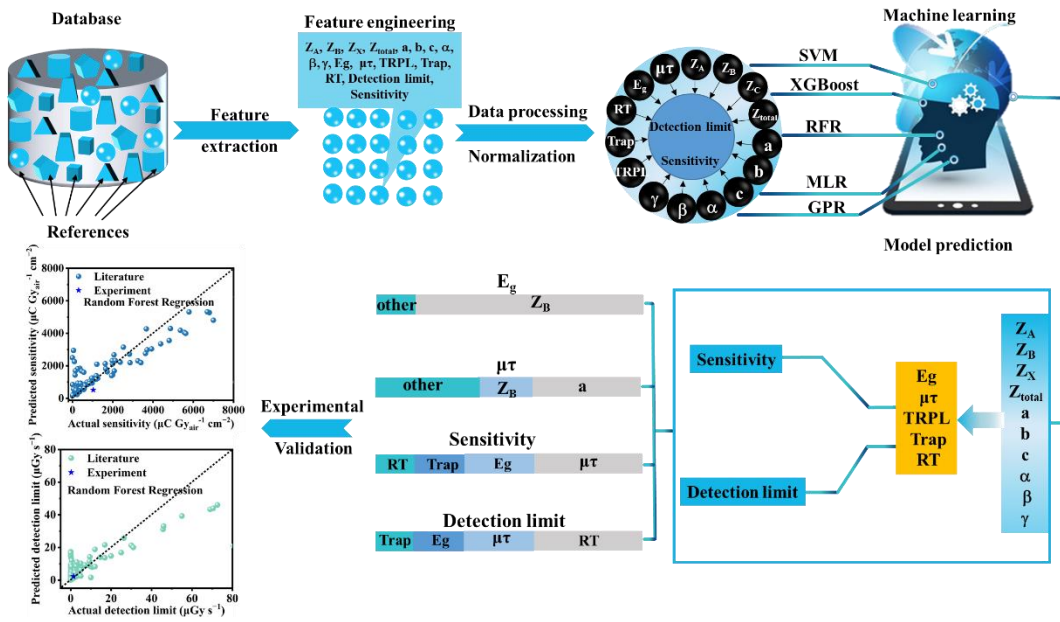


Figure 1. The workflow of this study. Firstly, relevant research papers are retrieved. Material data is extracted, and a database is generated. The database was used to train five machine learning models. The prediction results are further verified by experiments.

The main contributions of this study are summarized as following. First, a database of perovskite X-ray detector was created, containing 137 data samples and 23 features. The database is publicly open-source and can be further used by other researchers. Secondly, five different ML algorithms were applied to analyze the relationship between four target features (i.e., bandgap, carrier mobility-lifetime product, sensitivity, and detection limit) and other parameters (Figure 2), showing the applicability of ML into perovskite X-ray detector. Our new experimental material for X-ray detectors further verified the prediction accuracy of ML in the real-world settings. Finally, the analysis of different ML models reveals that the atomic number of B-site elements has the most profound impact on the E_g while lattice length b affects $\mu\tau$ mostly among other features. The data and codes are available at https://github.com/hed115599/ML_X-ray_Detector.

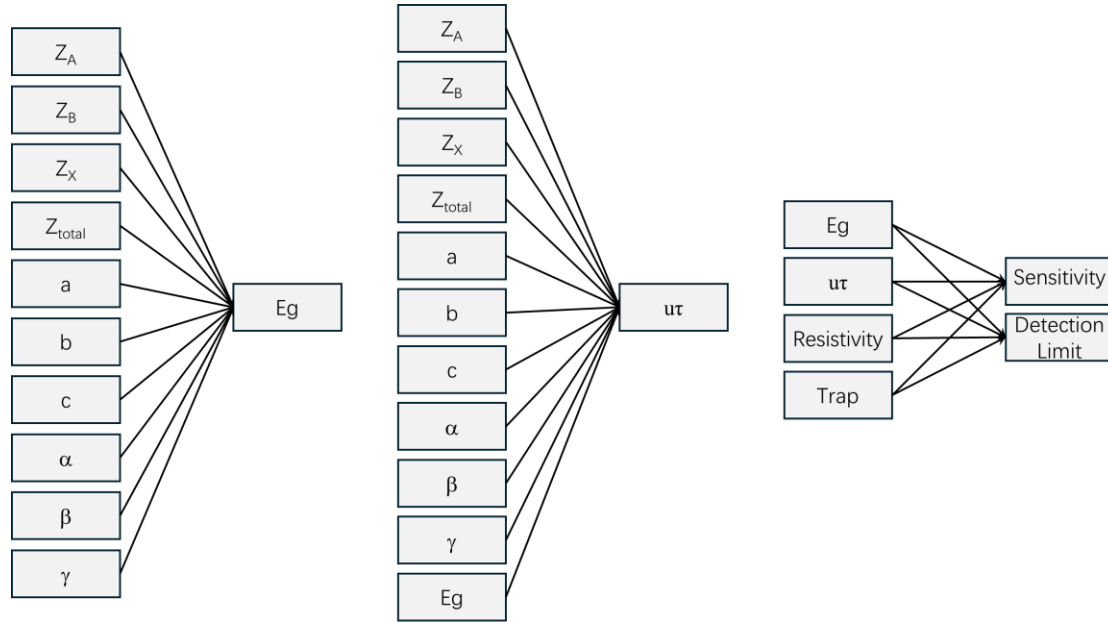


Figure 2. Four target features (bandgap, carrier mobility-lifetime product, sensitivity, and detection limit) and its dependent features to be analyzed.

2. Results and discussion

2.1. Database

The database is constructed from 136 relevant research papers and 1 real-world experiment conducted in this study. Each data sample contains 23 features, and the details are summarized in Table 1. During the data collection process, missing values (e.g., those not mentioned in the literature) are estimated using comparable values from other literature sources. To mitigate errors introduced by human factors, a diminished weight was applied to data samples containing estimated values when using the data (details provided in the Supplementary Information).

Table 1. Summary of the database.

Feature	Abbreviation	Mean	Max	Min
Perovskite	NA	NA	NA	NA
Molecular Structure	NA	NA	NA	NA
Atomic number of A site	Z_A	109.3	1678.0	18.0
Atomic number of B site	Z_B	181.2	209.0	18.0
Atomic number of X site	Z_X	105.0	127.0	35.5
Total atomic number	Z_{total}	1054.0	6443.0	210.5

lattice lengths/a(Å)	a	11.0	50.7	5.9
lattice lengths/b(Å)	b	10.0	32.5	4.8
lattice lengths/c(Å)	c	13.6	57.0	5.9
lattice angle/α°	α	89.4	105.1	24.9
lattice angle/β°	β	90.4	116.8	9.6
lattice angle/γ°	γ	94.9	120.0	9.4
Band gap (eV)	E _g	2.4	7.1	1.0
(cm²V⁻¹)	$\mu\tau$	2.1	200.0	1.1E-06
(cm²V⁻¹s⁻¹)	u	73.5	2652.0	2.0E-05
Resistivity((Ω cm)	RT	7.6E+11	6.3E+13	1.0E-10
Trap density(cm⁻³)	Trap	3.3E+14	2.5E+16	1.5E-11
TRPL(ns)	TRPL	4805.6	6.0E+05	0.5
Type	NA	NA	NA	NA
X-ray energy(KeV)		57.1	140.0	8.0
Applied electric filed (V mm⁻¹)		357.6	5000.0	0.0
Sensitivity (μCGy⁻¹ cm⁻²)		1.4E+05	5.2E+06	0.4
Detection limit (μGyair⁻¹ s⁻¹)		25.0	1200.0	2.0E-05

2.2. Machine learning prediction

To demonstrate the machine learning prediction, the Predicted vs. Actual Plot with training and test R^2 (RFR as an example) is shown in Figure 3. The x-axis represents the true values while the y-axis represents the predicted values output by the ML model. A closer alignment of points to the diagonal indicates a stronger correspondence between the model's predicted values and the actual values, reflecting the model's predictive accuracy. The training R^2 and test R^2 of the RFR model for E_g (Figure 3a) are 0.97 and 0.80, respectively. The scatter points locate closely to the diagonal. These demonstrate that the RFR model fits and predicts E_g well. However, for $\mu\tau$, sensitivity, and detection limit, both the training R^2 and test R^2 are relatively low, and the Predicted vs. Actual Plot shows errors (Figure 3b-3d). Other ML models also show similar results

(Figure S2-S5). Considering the low training R^2 and the substantial learning capabilities of these models, the current feature set may not adequately capture the essential predictors required for forecasting the target objectives. Additionally, the database used in this study was extracted from various literature sources. This aggregation of data from different experimental settings and instrumentation may introduce variability and errors that could further contribute to the observed low predictive accuracy. Further investigations into feature selection, as well as the exploration of additional features, may be necessary to enhance the model's predictive accuracy and these remain to be our future work.

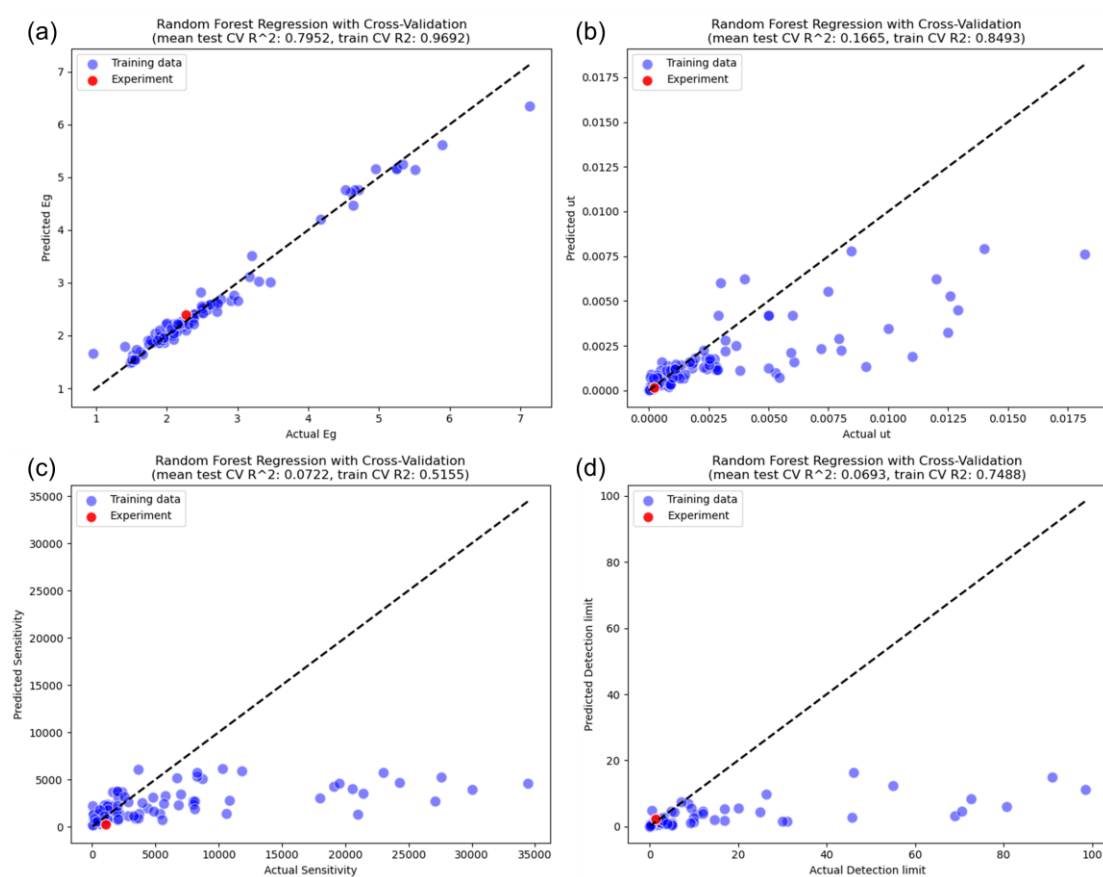


Figure 3. Predicted vs. Actual Plot of RFR for (a) Eg, (b) $\mu\tau$, (c) sensitivity, and (d) detection limit.

To further test the validity of our trained ML models in the real-world instead of only in literature, an experimental verification was conducted. It is noteworthy that 70% of the database is comprised of lead-based perovskite materials. Consequently, we have

opted to employ a low-dimensional lead-based perovskite material for experimental validation.

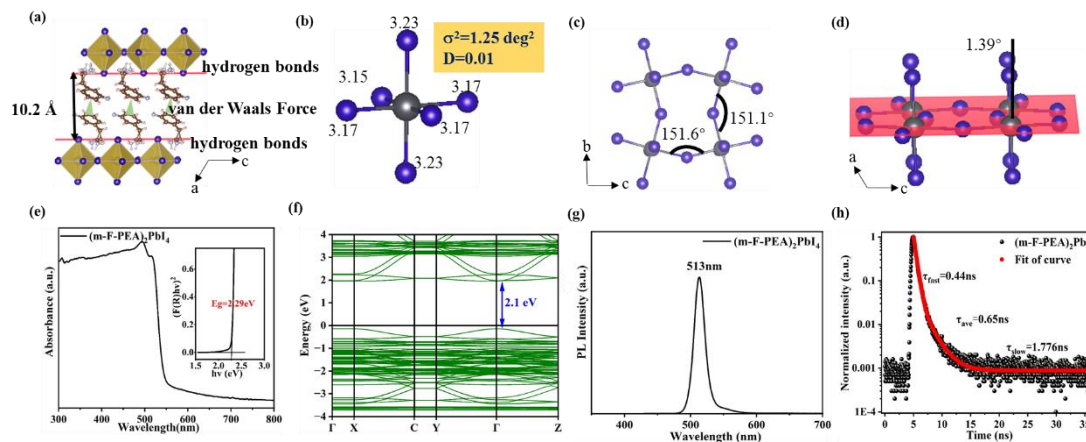


Figure 4. (a) Packing view along b-axis of $(m\text{-F-PEA})_2\text{PbI}_4$, red represents hydrogen bonding between organic and inorganic layers, and cyan represents the existence of van der Waals forces between organic ions. (b) Ball-and-stick model of lead iodine octahedron. (c) In-plane (Pb-I-Pb) and (d) out-of-plane distortion (quantitatively expressed as the residual angle of the angle formed by the Pb-I bond in the stacking direction and the layer plane) of $(m\text{-F-PEA})_2\text{PbI}_4$. (e) Absorption spectra, (f) band structure, (g) PL spectra and (h) the corresponding PL lifetime for the $(m\text{-F-PEA})_2\text{PbI}_4$.

The block-shaped orange-yellow single crystals $(m\text{-F-PEA})_2\text{PbI}_4$ (i.e., $20 \times 5 \times 0.7 \text{ mm}^3$) were grown through temperature cooling crystallization in a heated HI solution containing chemically reactive m-FPEA and PbO (Figure S7a). The results obtained from the scanning electron microscope (SEM) indicate that the surface of the single crystal is exceptionally smooth (Figure S7b), whereas the cross-sectional image (Figure S7c) reveals a periodic layered morphology. The results of the thermogravimetric analysis (TGA) and corresponding first derivative results indicated that the mass loss of $(m\text{-F-PEA})_2\text{PbI}_4$ was as low as 1% at a temperature of up to 240°C (Figure S8a,b), which surpasses many hybrid perovskite counterparts, such as $(\text{PEA})_2\text{PbI}_4$ (215°C , PEA = phenethylammonium)¹⁹, DABCO- NH_4Cl (208.9°C , DABCO = N-N'-diazabicyclo[2.2.2]octonium)²⁰. The simulated patterns align closely with the powder X-ray diffraction (XRD) patterns of $(m\text{-F-PEA})_2\text{PbI}_4$ (Figure S8c). The periodic XRD peaks observed in the $(m\text{-F-PEA})_2\text{PbI}_4$ SCs confirm the presence of a layered crystal structure and its growth along the (002) crystal face orientation (Figure S8d). The

precise crystal structure of (m-F-PEA)₂PbI₄ was determined by single crystal X-ray diffraction, as shown in Figure 4, and detailed crystallographic data are provided in Table S2. The crystallographic analysis reveals that the crystal structure of (m-F-PEA)₂PbI₄ is a typical Ruddlesden–Popper (RP) phase, adopting the C2/c space group (a=66.489(4) Å, b=12.2142(6) Å, c=12.2131(8) Å). The inorganic layers are separated by two large organic cations, with van der Waals forces acting between the organic layers. The organic layers are primarily connected to the inorganic layers through hydrogen bonding (Figure 4a).

The electronic structure of perovskites is primarily determined by the PbI₆ octahedron that make up the inorganic layer. Consequently, any distortion in the octahedra would affect their optoelectronic properties, such as the absorption/emission of excitons.³⁸ Octahedral distortion can be quantitatively evaluated using the distortion index (D) and the bond angle variance (σ²):

$$D = \frac{1}{6} \sum_1^6 \frac{|L_i - L_{av}|}{L_{av}} \quad (1)$$

$$\sigma^2 = \sum_1^{12} \frac{(\theta_i - 90)^2}{11} \quad (2)$$

The variables L_i and L_{av} represent the individual and average Pb–I bond length, respectively, while θ_i denotes the individual I–Pb–I angle. The presence of smaller σ (1.25 deg²) and D (0.01) values in (m-F-PEA)₂PbI₄ indicates a narrower fluorescent emission spectrum (Figure 4b).³⁹ The band gap is acknowledged to be influenced by the Pb–I–Pb bond angles, whereby smaller angles contribute to a reduced overlap between the Pb 6s and I 5p orbitals, consequently yielding a higher band gap.⁴⁰ The compounds (m-F-PEA)₂PbI₄ (151.1°) and (o-F-PEA)₂PbI₄ (150.9°)⁴¹ exhibit comparable Pb–I–Pb bond angles, resulting in a nearly identical band gap (2.29 eV) (Figure 4c and Figure 4e). The band gap (2.10 eV) obtained from density functional theory (DFT) calculations is in close agreement with the experimental results (Figure 4f). Furthermore, the smaller out-of-plane distortion of single-layer perovskites (1.39°) results in narrow-spectrum fluorescence with small Stokes shifts (Figure 4d and Figure 4g).

For semiconductor detectors, the trap density and the bulk resistivity of the

semiconductor material significantly affect the sensitivity and detection limit of the detector. This is particularly important for X-ray detectors that operate under high electric fields. A low trap density is advantageous for improving the sensitivity of the detector, while a high bulk resistivity is beneficial for enhancing the signal-to-noise ratio of the detector and consequently reducing the detection limit. We initially employed an impedance analyzer to test the capacitance-frequency curve of the (m-F-PEA)₂PbI₄ SC devices in the frequency range of 0.4 to 1 MHz, in a dark environment, for the purpose of calculating the relative dielectric constant (ϵ) of the single crystal (Figure S9a). ϵ of the single crystal was then calculated to be 6.0 ± 0.4 (Figure S9b). Subsequently, the I-V curve of the (m-F-PEA)₂PbI₄ SC under dark conditions was analyzed using the Keysight B2912A precision source meter, and evaluated based on the SCLC model (Figure S9c). The defect density of (m-F-PEA)₂PbI₄ SC is $6.4 \times 10^{10} \text{ cm}^{-3}$, comparable to that of previously reported 3D⁴² and 2D⁷ metal halide SCs and significantly lower than traditional semiconductor materials such as Si⁴³ and CdTe⁴⁴. Additionally, the carrier mobility ($9.76 \times 10^{-2} \text{ cm}^2 \text{ V}^{-1} \text{ s}^{-1}$) of (m-F-PEA)₂PbI₄ SC was obtained by analyzing the "child" segment of the dark I-V curve. As shown in Figure S9d, the (m-F-PEA)₂PbI₄ SC demonstrates a significant bulk resistivity of $3.78 \times 10^{11} \text{ } \Omega \text{ cm}$, which serves to effectively suppress leakage current and mitigate the impact of noise current.

In order to investigate the X-ray detection capabilities of (m-F-PEA)₂PbI₄, the X-ray absorption coefficients for perovskite and conventional semiconductor materials in the photon energy range of 10keV to 1.1MeV were calculated using the NIST X-COM database.⁴⁵ The absorption coefficient of (m-F-PEA)₂PbI₄ is significantly higher than silicon across the entire energy spectrum of the display, rivaling α -Se and other similar 2D perovskite materials (Figure S10a). On this basis, we further calculate the thickness required for different materials to fully absorb a fixed energy of X-rays. As shown in Figure S10b, it can be observed that a single crystal of (m-F-PEA)₂PbI₄ with a thickness of 0.7 mm can absorb 94% of the peak energy of X-rays at 40 keV. Furthermore, based on the modified Hecht equation, the current-voltage (I-V) curve of the (m-F-PEA)₂PbI₄ SC device under X-ray irradiation was fitted, yielding a mobility-lifetime ($\mu\tau$) product

of $1.81 \times 10^{-4} \text{ cm}^2 \text{ V}^{-1}$, which is comparable to that of 3D MAPbBr₃ ($2.6 \times 10^{-4} \text{ cm}^2 \text{ V}^{-1}$)⁴⁶ and significantly higher than that of α -Se ($10^{-7} \text{ cm}^2 \text{ V}^{-1}$)⁴⁷ (Figure S11a). Moreover, there are significant variations in the dark I-V and illumination I-V, demonstrating the favorable response of the (m-F-PEA)₂PbI₄ SC device to X-rays (Figure S11b).

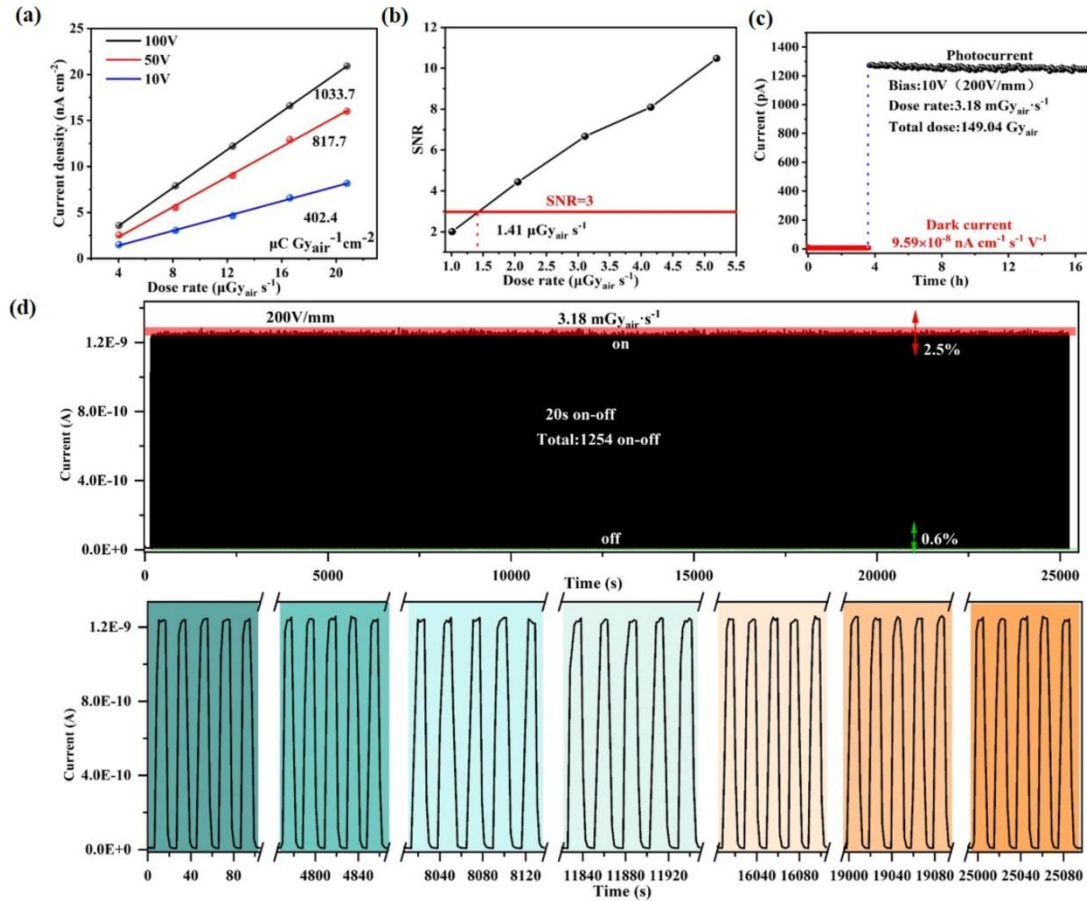


Figure 5. (a) Sensitivity fitting of the (m-F-PEA)₂PbI₄ SC detector under different bias voltage. (b) Signal to noise ratio (SNR) of the (m-F-PEA)₂PbI₄ SC detector under different dose rates at 100 V bias. (c) Dark current drift and radiation stability (under continuous X-ray irradiation for more than 12 hours) measurement of the (m-F-PEA)₂PbI₄ SC detector. (d) (m-F-PEA)₂PbI₄ SC detector switch stability test and 7 local magnification images.

Through the utilization of the exceptional charge transfer properties within the plane of two-dimensional perovskites, a coplanar detector was fabricated based on the (m-F-PEA)₂PbI₄ SC, and its X-ray detection performance was evaluated using sensitivity and detection limit. Figure S12a shows the on/off photocurrent response curve of the (m-F-PEA)₂PbI₄ SC X-ray detector at bias voltages from 10 V to 100 V and at X-ray doses from 2.7 μGy s⁻¹ to 22.7 μGy s⁻¹. The sensitivity at different bias

voltages was calculated from the photocurrent on/off response curves as shown in Figure 5a, and reached $1033.7 \mu\text{C Gy}_{\text{air}}^{-1} \text{cm}^{-2}$ at a bias voltage of 100 V. The sensitivity of this value is higher than that of a 2D perovskite $(\text{PEA})_2\text{PbI}_4$ SC X-ray detector ($848 \mu\text{C Gy}_{\text{air}}^{-1} \text{cm}^{-2}$)¹⁹, and 51.7 times higher than the sensitivity of the current commercially available α -Se X-ray detector used for X-ray imaging under high electric field (10000 V mm^{-1}) ($20 \mu\text{C Gy}_{\text{air}}^{-1} \text{cm}^{-2}$).⁴⁷ Moreover, the response current of the $(\text{m-F-PEA})_2\text{PbI}_4$ SC detector at low X-ray dose rates was tested for the calculation of the detection limit (Figure S12b). As illustrated in Figure 5b, we calculated and fitted the X-ray dose rate versus detector signal-to-noise ratio (SNR) and extended the fit line to an SNR of 3 (as defined by the International Union of Pure and Applied Chemistry⁴⁸) to determine the detection limit of $1.41 \mu\text{Gy s}^{-1}$ for the $(\text{m-F-PEA})_2\text{PbI}_4$ SC detector, which is nearly 4 times lower than the dose rate used in conventional medical diagnostics ($5.5 \mu\text{Gy s}^{-1}$).⁴⁹ The lower detection limit can significantly reduce the radiation dose received by patients during routine X-ray examinations, thereby greatly reducing the risk of X-ray exposure.

The stability and repeatability of detectors in different environments are crucial indicators for evaluating their usability in practical applications. Initially, under the continuous application of an electric field of 200 V mm^{-1} , we conducted a dark current test on $(\text{m-F-PEA})_2\text{PbI}_4$ SC devices for nearly 4 hours (Figure 5c). The dark current drift of the 2D $(\text{m-F-PEA})_2\text{PbI}_4$ SC detector is $9.59 \times 10^{-8} \text{ nA cm}^{-1} \text{ s}^{-1} \text{ V}^{-1}$, which is significantly lower by five orders of magnitude compared to the dark current drift of the 3D MAPbI_3 SC detector ($2.0 \times 10^{-3} \text{ nA cm}^{-1} \text{ s}^{-1} \text{ V}^{-1}$).⁵⁰ This remarkable improvement is attributed to the extremely low ion migration of the 2D $(\text{m-F-PEA})_2\text{PbI}_4$ SC. Furthermore, the $(\text{m-F-PEA})_2\text{PbI}_4$ SC detector can operate for more than 12 hours under high doses and continuous X-ray irradiation, with no significant decrease in X-ray response current, indicating that it is intrinsically structurally stable under X-ray irradiation (Figure 5c). We also conducted tests on the stability of the $(\text{m-F-PEA})_2\text{PbI}_4$ SC X-ray detector when exposed to air at room temperature (Figure S13a). The results indicate that the response current of the detector remains comparable to the initial response value, even under different high doses ($96.2\text{-}790.2 \mu\text{Gy s}^{-1}$) after 60

days (Figure S13b). Finally, after 1254 response cycles at 20 seconds interval, the response current and dark current of the (m-F-PEA)₂PbI₄ SC detector remained 97.5% and 99.45% of the initial value, respectively (Figure 5d). During a testing period of over 25000s, the on-off response of seven magnified sections remained consistent, further indicating the device has excellent on-off stability. The response time of detectors has been investigated due to the rapid response of X-rays, which can reduce the radiation dose received by patients in medical diagnosis. The rise time (from 10% to 90%) of the (m-F-PEA)₂PbI₄ SC detector for pulsed X-ray is measured to be 16.8 ms, while the fall time (from 90% to 10%) is determined to be 29.1 ms (Figure S14). Combining good X-ray detection properties with excellent stability, (m-F-PEA)₂PbI₄ SC hold promise for high-quality X-ray imaging.

The experimental result above is visualized in Figure 3 (red dot). The RFR model predicted a bandgap value as 2.23 eV, which is closest to the experimental value (2.29 eV), followed by XGBoost (2.42 eV), GPSR (2.09 eV), SVR (2.56 eV), and MLR (1.98 eV) (Figure 3a and Figure S6a). Compared to the DFT calculation result (2.1 eV), the prediction by machine learning models is more accurate. Despite the low fitting accuracy of $\mu\tau$ and detection limit, the RFR model still predicted these targets with considerable accuracy (Figure 3b and 3d). For sensitivity, there is a slight error between the experimental value and the predicted value (Figure 3c).

2.3. Machine learning analysis

To determine which feature has the most significant impact on the target, we ranked the feature importance (calculated using permutation importance) within each ML model (Figure 6). The ranking reveals that the Z_B has most significant effect on E_g with a highest feature importance among other features. This finding is consistent with the high Pearson correlation coefficient (-0.85) between E_g and Z_B (Figure 6a). The B-sites occupying the perovskites in the collected database are dominated by the elements Pb, Bi and small organic molecules (NH_4^+ , $N_2H_4^+$). Perovskites incorporating small organic molecules at the B-site are classified as molecular perovskites²⁹. The organic constituents of these molecular perovskites play a significant role in determining the

band gap. Typically, organic molecules exhibit a wide band, and the weak interaction between organic macromolecules and halogens leads to a relatively large energy discrepancy (i.e., band gap) between the valence and conduction bands^{14, 21, 30}.

The GPSR model can provide a formula for predicting bandgaps that

$$E_g = \log(Z_B \times Z_X) + \sqrt{Z_B} \quad (3)$$

where Z_B and Z_X represent the atomic numbers of the B-site and X-site atoms in organic-inorganic hybrid halide perovskites. The formula also indicates the high relationship between Z_B and E_g . According to formula 1, the bandgap of perovskites is related to the B and X site atoms but not to the A atom, aligning with the fact that A-site ions do not directly contribute to the band structure in actual perovskites³⁷.

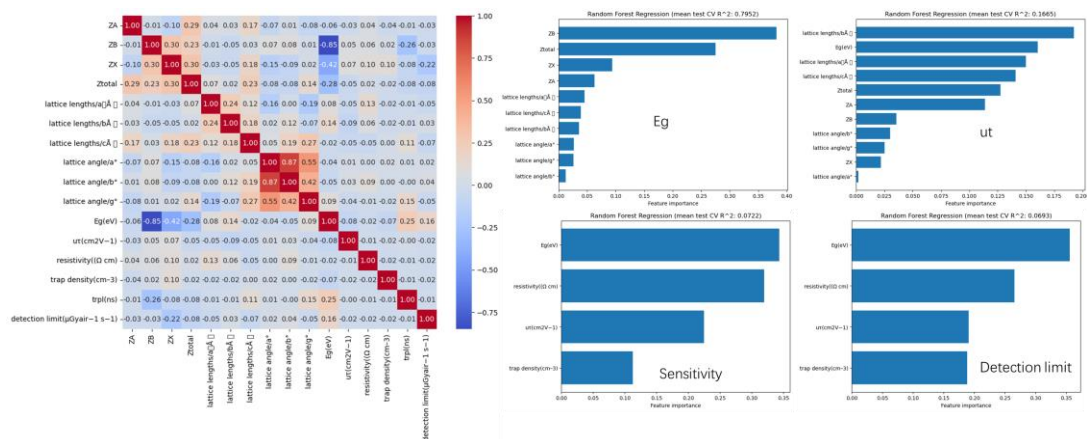


Figure 6. The Pearson correlation heatmap (a) and feature importance ranking for E_g (b), $\mu\tau$ (c), sensitivity (d), and detection limit (e).

Despite the low test R^2 for $\mu\tau$, most of ML models weight more on lattice length b in prediction of $\mu\tau$ (Figure 6c). Among the five ML models, RFR has demonstrated a remarkable ability to predict the properties of perovskite X-ray detectors with high accuracy (Table S1). This robust performance can be attributed to several inherent characteristics of the RFR algorithm and the specific nature of perovskite materials and their properties. Firstly, perovskite materials exhibit complex and non-linear relationships between their structural parameters. RFR is particularly adept at capturing these non-linear interactions without the need for explicit model specification, unlike linear regression models. This capability allows RFR to model the nuanced impacts of compositional and structural variations in perovskites more effectively. Secondly, our

datasets may contain outliers or missing values due to experimental challenges and variability in synthesis conditions. RFR is capable of handling such datasets effectively, as the random forest algorithm is less sensitive to outliers and can handle missing data by using surrogate splits or ignoring missing values during the node splitting in trees. Therefore, given these strengths, we suggest further utilization and investigation of RFR for researchers and developers in the field of X-ray detector.

CONCLUSION

In this work, we collected a database for perovskite X-ray detectors and demonstrated that ML techniques can be applied to analyze parameters in perovskite X-ray detectors. Five ML regression models were trained to analyze the main factors affecting E_g , $\mu\tau$, sensitivity, and detection limit. The RFR model has identified the intrinsic parameter Z_B of a given perovskite material to have the greatest impact on the E_g , while lattice length b affects $\mu\tau$ mostly among the features. The obtained result aligns with its corresponding physical significance, revealing the applicability of the ML model. Our ultimately prepared (m-F-PEA)₂PbI₄ single-crystal X-ray detectors further verified the accuracy of ML models in real-world applications. We suggest further studies on RFR for X-ray detector applications.

ASSOCIATED CONTENT

Supporting Information

The supporting information is free of charge via the Internet at <http://pubs.acs.org>.

Experimental procedures, synthesis procedure, material characterization, molecular polarity calculation, computational methods, dielectric measurement, SCLC measurement, photoconductivity analysis, X-ray detector performance measurements, X-ray imaging and additional crystallographic data (PDF)

Author contributions

J.Y. conceived the project and wrote the original manuscript. J.Y. supervised the project. B.Z. conducted most of experiments and co-wrote the paper. E.H. performed machine learning analysis. All authors discussed and analyzed the data.

Notes

The authors declare no competing financial interest.

ACKNOWLEDGEMENTS

This work was funded by the Strategic Priority Research Program of the Chinese Academy of Sciences (Grant No. XDA17040506), the National Key Research and Development Program of China (2017YFA0204800), the Key Program project of the National Natural Science Foundation of China (51933010), the National Natural Science Foundation of China (61974085/51901190), the 111 Project (B21005), the Young Scientist Initiative Project of School of Materials Science and Engineering at Shaanxi Normal University (SNNU) (2022YSIP-MSE-SNNU001), the Changjiang Scholars and Innovative Research Team (IRT14R33) and the National University Research Fund (GK202103113). A.K.Y.J. thanks the sponsorship of the Lee Shau-Kee Chair Professor (Materials Science), and the support from the APRC Grants (9380086, 9610419, 9610492, 9610508) of the City University of Hong Kong, the TCFS Grant (GHP/018/20SZ) and MRP Grant (MRP/040/21X) from the Innovation and Technology Commission of Hong Kong, the Green Tech Fund (202020164) from the Environment and Ecology Bureau of Hong Kong, the GRF grants (11307621, 11316422) from the Research Grants Council of Hong Kong, Shenzhen Science and Technology Program (SGDX20201103095412040), Guangdong Major Project of Basic and Applied Basic Research (2019B030302007).

REFERENCES

- (1) He, X.; Deng, Y.; Ouyang, D.; Zhang, N.; Wang, J.; Murthy, A. A.; Spanopoulos, I.; Islam, S. M.; Tu, Q.; Xing, G.; Li, Y.; Dravid, V. P.; Zhai, T. Recent Development of Halide Perovskite Materials and Devices for Ionizing Radiation Detection. *Chem Rev.* **2023**, *123*, 1207-1261.
- (2) Yakunin, S.; Sytnyk, M.; Kriegner, D.; Shrestha, S.; Richter, M.; Matt, G. J.; Azimi, H.; Brabec, C. J.; Stangl, J.; Kovalenko, M. V.; Heiss, W. Detection of X-ray photons by solution-processed organic-inorganic perovskites. *Nat. Photonics* **2015**, *9*, 444-449.
- (3) Guan, Q.; You, S.; Zhu, Z. K.; Li, R.; Ye, H.; Zhang, C.; Li, H.; Ji, C.; Liu, X.; Luo, J. Three-Dimensional Polar Perovskites for Highly Sensitive Self-Driven X-Ray Detection. *Angew. Chem. Int. Ed.* **2024**, e202320180.
- (4) Wu, H.; Ge, Y.; Niu, G.; Tang, J. Metal Halide Perovskites for X-Ray Detection and Imaging. *Matter* **2021**, *4*, 144-163.
- (5) Jin, P.; Tang, Y.; Li, D.; Wang, Y.; Ran, P.; Zhou, C.; Yuan, Y.; Zhu, W.; Liu, T.; Liang, K.; Kuang, C.; Liu, X.; Zhu, B.; Yang, Y. M. Realizing nearly-zero dark current and ultrahigh signal-to-noise ratio perovskite X-ray detector and image array by dark-current-shunting strategy. *Nat. Commun.* **2023**, *14*, 626.
- (6) Li, H.; Song, J.; Pan, W.; Xu, D.; Zhu, W. A.; Wei, H.; Yang, B. Sensitive and Stable 2D Perovskite Single-Crystal X-ray Detectors Enabled by a Supramolecular Anchor. *Adv. Mater.* **2020**, *32*, e2003790.
- (7) Xia, M.; Yuan, J. H.; Niu, G.; Du, X.; Yin, L.; Pan, W.; Luo, J.; Li, Z.; Zhao, H.; Xue, K. H.; Miao, X.; Tang, J. Unveiling the Structural Descriptor of A₃B₂X₉Perovskite Derivatives toward X-Ray Detectors with Low Detection Limit and High Stability. *Adv. Funct. Mater.* **2020**, *30*, 1910648.
- (8) Zhang, M.; Xin, D.; Dong, S.; Zhao, W.; Tie, S.; Cai, B.; Ma, Q.; Chen, Q.; Zhang, W. H.; Zheng, X. Methylamine-Assisted Preparation of Ruddlesden-Popper Perovskites for Stable Detection and Imaging of X-Rays. *Adv. Opt. Mater.* **2022**, 2201548.
- (9) Shen, Y.; Liu, Y.; Ye, H.; Zheng, Y.; Wei, Q.; Xia, Y.; Chen, Y.; Zhao, K.; Huang, W.; Liu, S. Centimeter-Sized Single Crystal of Two-Dimensional Halide Perovskites Incorporating Straight-Chain Symmetric Diammonium Ion for X-Ray Detection. *Angew. Chem. Int. Ed.* **2020**, *59*, 14896-14902.
- (10) Ma, C.; Gao, L.; Xu, Z.; Li, X.; Song, X.; Liu, Y.; Yang, T.; Li, H.; Du, Y.; Zhao, G.; Liu, X.; Kanatzidis, M. G.; Liu, S. F.; Zhao, K. Centimeter-Sized 2D Perovskitoid Single Crystals for Efficient X-ray Photoresponsivity. *Chem. Mater.* **2022**, *34*, 1699-1709.
- (11) Wang, Y.; Zhang, S.; Wang, Y.; Yan, J.; Yao, X.; Xu, M.; Lei, X. W.; Lin, G.; Yue, C. Y. 0D triiodide hybrid halide perovskite for X-ray detection. *Chem Commun (Camb)* **2023**, *59*, 9239-9242.
- (12) Xu, Y.; Hu, J.; Xiao, X.; He, H.; Tong, G.; Chen, J.; He, Y. Evaporation crystallization of zero-dimensional guanidinium bismuth iodide perovskite single crystal for X-ray detection. *Inorg. Chem. Front.* **2022**, *9*, 494-500.
- (13) Yang, X.; Huang, Y.-H.; Wang, X.-D.; Li, W.-G.; Kuang, D.-B. A-Site Diamine Cation Anchoring Enables Efficient Charge Transfer and Suppressed Ion Migration in Bi-Based Hybrid Perovskite Single Crystals. *Angew. Chem. Int. Ed.* **2022**, *61*, 202204663.
- (14) Song, X.; Cohen, H.; Yin, J.; Li, H.; Wang, J.; Yuan, Y.; Huang, R.; Cui, Q.; Ma, C.; Liu, S. F.; Hodes, G.; Zhao, K. Low Dimensional, Metal-Free, Hydrazinium Halide Perovskite-Related Single Crystals and Their Use as X-Ray Detectors. *Small* **2023**, *19*, e2300892.
- (15) Guo, J.; Xu, Y.; Yang, W.; Xiao, B.; Sun, Q.; Zhang, X.; Zhang, B.; Zhu, M.; Jie, W. High-

Stability Flexible X-ray Detectors Based on Lead-Free Halide Perovskite Cs(2)TeI(6) Films. *ACS Appl. Mater. Interfaces* **2021**, *13*, 23928-23935.

(16) Dong, K.; Zhou, H.; Shao, W.; Gao, Z.; Yao, F.; Xiao, M.; Li, J.; Liu, Y.; Wang, S.; Zhou, S.; Cui, H.; Qin, M.; Lu, X.; Tao, C.; Ke, W.; Fang, G. Perovskite-like Silver Halide Single-Crystal Microbelt Enables Ultrasensitive Flexible X-ray Detectors. *ACS Nano* **2023**, *17*, 1495-1504.

(17) Fan, Q.; Xu, H.; You, S.; Ma, Y.; Liu, Y.; Guo, W.; Hu, X.; Wang, B.; Gao, C.; Liu, W.; Luo, J.; Sun, Z. Centimeter-Sized Single Crystals of Dion-Jacobson Phase Lead-Free Double Perovskite for Efficient X-ray Detection. *Small* **2023**, *19*, e2301594.

(18) Wu, J.; You, S.; Yu, P.; Guan, Q.; Zhu, Z.-K.; Li, Z.; Qu, C.; Zhong, H.; Li, L.; Luo, J. Chirality Inducing Polar Photovoltage in a 2D Lead-Free Double Perovskite toward Self-Powered X-ray Detection. *ACS Energy Lett.* **2023**, *8*, 2809-2816.

(19) Zhang, B.; Xu, Z.; Ma, C.; Li, H.; Liu, Y.; Gao, L.; Zhang, J.; You, J.; Liu, S. First-Principles Calculation Design for 2D Perovskite to Suppress Ion Migration for High-Performance X-ray Detection. *Adv. Funct. Mater.* **2022**, *32*, 2110392.

(20) Cui, Q.; Song, X.; Liu, Y.; Xu, Z.; Ye, H.; Yang, Z.; Zhao, K.; Liu, S. Halide-modulated self-assembly of metal-free perovskite single crystals for bio-friendly X-ray detection. *Matter* **2021**, *4*, 2490-2507.

(21) Li, Z.; Li, Z.; Peng, G.; Shi, C.; Wang, H.; Ding, S. Y.; Wang, Q.; Liu, Z.; Jin, Z. PF(6) (-) Pseudohalides Anion based Metal-Free Perovskite Single Crystal for Stable X-ray Detector to Attain Record Sensitivity. *Adv. Mater.* **2023**, *35*, e2300480.

(22) Song, Y.; Li, L.; Hao, M.; Bi, W.; Wang, A.; Kang, Y.; Li, H.; Li, X.; Fang, Y.; Yang, D.; Dong, Q. Elimination of Interfacial-electrochemical-reaction-induced Polarization in Perovskite Single Crystals for Ultra-sensitive and Stable X-ray Detector Arrays. *Adv. Mater.* **2021**, *33*, e2103078.

(23) Shen, Y.; Ran, C.; Dong, X.; Wu, Z.; Huang, W. Dimensionality Engineering of Organic-Inorganic Halide Perovskites for Next-Generation X-Ray Detector. *Small* **2023**, e2308242.

(24) He, Y.; Hadar, I.; Kanatzidis, M. G. Detecting ionizing radiation using halide perovskite semiconductors processed through solution and alternative methods. *Nat. Photonics* **2021**, *16*, 14-26.

(25) Lu, S.; Zhou, Q.; Ouyang, Y.; Guo, Y.; Li, Q.; Wang, J. Accelerated discovery of stable lead-free hybrid organic-inorganic perovskites via machine learning. *Nat. Commun.* **2018**, *9*, 3405.

(26) Yu, Y.; Tan, X.; Ning, S.; Wu, Y. Machine Learning for Understanding Compatibility of Organic-Inorganic Hybrid Perovskites with Post-Treatment Amines-SVM. *ACS Energy Lett.* **2019**, *4*, 397-404.

(27) Hu, Y.; Hu, X.; Zhang, L.; Zheng, T.; You, J.; Jia, B.; Ma, Y.; Du, X.; Zhang, L.; Wang, J.; Che, B.; Chen, T.; Liu, S. Machine-Learning Modeling for Ultra-Stable High-Efficiency Perovskite Solar Cells. *Adv. Energy Mater.* **2022**, 2201463.

(28) Zhi, C.; Wang, S.; Sun, S.; Li, C.; Li, Z.; Wan, Z.; Wang, H.; Li, Z.; Liu, Z. Machine-Learning-Assisted Screening of Interface Passivation Materials for Perovskite Solar Cells. *ACS Energy Lett.* **2023**, *8*, 1424-1433.

(29) Song, X.; Cui, Q.; Liu, Y.; Xu, Z.; Cohen, H.; Ma, C.; Fan, Y.; Zhang, Y.; Ye, H.; Peng, Z.; Li, R.; Chen, Y.; Wang, J.; Sun, H.; Yang, Z.; Liu, Z.; Yang, Z.; Huang, W.; Hodes, G.; Liu, S. F.; Zhao, K. Metal-Free Halide Perovskite Single Crystals with Very Long Charge Lifetimes for Efficient X-ray Imaging. *Adv. Mater.* **2020**, *32*, e2003353.

(30) Cui, Q.; Liu, X.; Li, N.; Zeng, H.; Chu, D.; Li, H.; Song, X.; Xu, Z.; Liu, Y.; Zhu, H.; Zhao, K.;

- Liu, S. F. A New Metal-Free Molecular Perovskite-Related Single Crystal with Quantum Wire Structure for High-Performance X-Ray Detection. *Small* **2023**, e2308945.
- (31) Chu, D.; Jia, B.; Liu, N.; Zhang, Y.; Li, X.; Feng, J.; Pi, J.; Yang, Z.; Zhao, G.; Liu, Y.; Liu, S.; Park, N.-G. Lattice engineering for stabilized black FAPbI₃ perovskite single crystals for high-resolution x-ray imaging at the lowest dose. *Sci. Adv.* **2023**, *9*, eadh2255.
- (32) Li, X.; Zhang, G.; Hua, Y.; Cui, F.; Sun, X.; Liu, J.; Liu, H.; Bi, Y.; Yue, Z.; Zhai, Z.; Xia, H.; Tao, X. Dimensional and Optoelectronic Tuning of Lead-free Perovskite Cs₃Bi₂I_{9-n}Br_n Single Crystals for Enhanced Hard X-ray Detection. *Angew. Chem. Int. Ed.* **2023**, e202315817.
- (33) Sánchez-Palencia, P.; García, G.; Wahnón, P.; Palacios, P. Cation substitution effects on the structural, electronic and sun-light absorption features of all-inorganic halide perovskites. *Inorg. Chem. Front.* **2022**, *9*, 1337-1353.
- (34) Huang, Y.; Qiao, L.; Jiang, Y.; He, T.; Long, R.; Yang, F.; Wang, L.; Lei, X.; Yuan, M.; Chen, J. A-site Cation Engineering for Highly Efficient MAPbI₃ Single-Crystal X-ray Detector. *Angew. Chem. Int. Ed.* **2019**, *58*, 17834-17842.
- (35) Li, H.; Shen, N.; Chen, S.; Guo, F.; Xu, B. Recent Progress on Synthesis, Intrinsic Properties and Optoelectronic Applications of Perovskite Single Crystals. *Adv. Funct. Mater.* **2023**, *33*, 2214339.
- (36) Li, W.; Feng, X.; Guo, K.; Pan, W.; Li, M.; Liu, L.; Song, J.; He, Y.; Wei, H. Prominent Free Charges Tunneling Through Organic Interlayer of 2D Perovskites. *Adv. Mater.* **2023**, *35*, e2211808.
- (37) Xin, B.; Alaal, N.; Mitra, S.; Subahi, A.; Pak, Y.; Almalawi, D.; Alwadai, N.; Lopatin, S.; Roqan, I. S. Identifying Carrier Behavior in Ultrathin Indirect-Bandgap CsPbX₃ Nanocrystal Films for Use in UV/Visible-Blind High-Energy Detectors. *Small* **2020**, *16*, e2004513.
- (38) Du, K. Z.; Tu, Q.; Zhang, X.; Han, Q.; Liu, J.; Zauscher, S.; Mitzi, D. B. Two-Dimensional Lead(II) Halide-Based Hybrid Perovskites Templated by Acene Alkylamines: Crystal Structures, Optical Properties, and Piezoelectricity. *Inorg. Chem.* **2017**, *56*, 9291-9302.
- (39) Cortecchia, D.; Neutzner, S.; Srimath Kandada, A. R.; Mosconi, E.; Meggiolaro, D.; De Angelis, F.; Soci, C.; Petrozza, A. Broadband Emission in Two-Dimensional Hybrid Perovskites: The Role of Structural Deformation. *J. Am. Chem. Soc.* **2017**, *139*, 39-42.
- (40) Gao, L.; Li, X.; Traore, B.; Zhang, Y.; Fang, J.; Han, Y.; Even, J.; Katan, C.; Zhao, K.; Liu, S.; Kanatzidis, M. G. m-Phenylenediammonium as a New Spacer for Dion-Jacobson Two-Dimensional Perovskites. *J. Am. Chem. Soc.* **2021**, *143*, 12063-12073.
- (41) Zhang, B.; Zheng, T.; You, J.; Ma, C.; Liu, Y.; Zhang, L.; Xi, J.; Dong, G.; Liu, M.; Liu, S. Electron-Phonon Coupling Suppression by Enhanced Lattice Rigidity in 2D Perovskite Single Crystals for High-Performance X-Ray Detection. *Adv. Mater.* **2023**, *35*, 2208875.
- (42) Shi, R.; Pi, J.; Chu, D.; Jia, B.; Zhao, Z.; Hao, J.; Zhang, X.; Dong, X.; Liang, Y.; Zhang, Y.; Liu, Y.; Liu, S. Promoting Band Splitting through Symmetry Breaking in Inorganic Halide Perovskite Single Crystals for High-Sensitivity X-ray Detection. *ACS Energy Lett.* **2023**, *8*, 4836-4847.
- (43) Liu, X.; Zhang, H.; Zhang, B.; Dong, J.; Jie, W.; Xu, Y. Charge Transport Behavior in Solution-Grown Methylammonium Lead Tribromide Perovskite Single Crystal Using α Particles. *J. Phys. Chem. C* **2018**, *122*, 14355-14361.
- (44) Balcioglu, A.; Ahrenkiel, R. K.; Hasoon, F. Deep-level impurities in CdTe/CdS thin-film solar cells. *J. Appl. Phys.* **2000**, *88*, 7175-7178.
- (45) M.J. Berger, J. H. H., S.M. Seltzer, J. Chang, J.S. Coursey, R. Sukumar, D.S. Zucker, and K.

Olsen. *XCOM: photon cross sections database*, National Institute of Standards and Technology (NIST). <http://www.nist.gov/pml/data/xcom/index.cfm> (accessed 2023.08.01).

(46) Li, L.; Liu, X.; Zhang, H.; Zhang, B.; Jie, W.; Sellin, P. J.; Hu, C.; Zeng, G.; Xu, Y. Enhanced X-ray Sensitivity of MAPbBr₃ Detector by Tailoring the Interface-States Density. *ACS Appl. Mater. Interfaces* **2019**, *11*, 7522-7528.

(47) Kasap, S. O. X-ray sensitivity of photoconductors: application to stabilized α -Se. *J. Phys. D: Appl. Phys* **2000**, *33*, 2853-2865.

(48) Thompson, M.; Ellison, S. L. R.; Wood, R. Harmonized guidelines for single-laboratory validation of methods of analysis - (IUPAC technical report). *Pure Appl. Chem.* **2002**, *74*, 835-855.

(49) Shearer, D. R.; Bopaiah, M. Dose rate limitations of integrating survey meters for diagnostic X-ray surveys. *Health Phys.* **2000**, *79*, S20-S21.

(50) Liu, Y.; Xu, Z.; Yang, Z.; Zhang, Y.; Cui, J.; He, Y.; Ye, H.; Zhao, K.; Sun, H.; Lu, R.; Liu, M.; Kanatzidis, M. G.; Liu, S. Inch-Size 0D-Structured Lead-Free Perovskite Single Crystals for Highly Sensitive Stable X-Ray Imaging. *Matter* **2020**, *3*, 180-196.